Fuel 363 (2024) 130973

Contents lists available at ScienceDirect

Fuel

journal homepage: www.elsevier.com/locate/fuel

Full length article

Coupling radiative properties with detailed char conversion kinetics

Matthias Koch [a,*], Stefan Pielsticker [a], David Tarlinski [b], Viktor Scherer [b], Reinhold Kneer [a]

[a] Institute of Heat and Mass Transfer (WSA), RWTH Aachen University, Augustinerbach 6, 52056 Aachen, Germany
[b] Institute of Energy Plant Technology, Ruhr-University Bochum, Universitätsstraße 150, 44780 Bochum, Germany

ARTICLE INFO

Dataset link: https://doi.org/10.18154/RWTH-2023-09827

Keywords:
Conversion
Particle radiation
Burnout dependent particle radiation

ABSTRACT

In pulverized solid fuel combustion, radiation is the primary heat transfer mechanism. Especially in the near-burner region with high particle loadings, particle radiation dominates gas radiation. Thus, adequate modeling of particle-radiation interactions in full-scale simulations of combustion chambers may primarily affect the overall accuracy. The radiation behavior depends strongly on the particles? optical properties, characterized by the complex index of refraction (IOR). The IOR depends on particle morphology and material composition which change during pyrolysis and char conversion. For char conversion, the focus of the present paper, the change depends on how the structural transformations take place inside the particle, characterizes by the reaction regimes, boundary layer diffusion limited, pore diffusion limited or kinetically controlled. The formation of an outer ash film layer with progressing burnout can complicate the situation even more.

To quantify the effects of the structural changes during the char conversion process on the radiative properties, the output data of the char conversion kinetics (CCK) model (particle size, ash/carbon content, pore fraction) are used to build artificial particles at different conversion degrees and for the different regimes. Finally, the radiation interaction is calculated by applying an extension of the Mie theory for coated particles, and these results are compared to simplified approaches.

Simplified approaches were tested to derive the IOR by applying mixing rules based on the available char and ash content with progressing char conversion. The results indicate that only a non-linear mixing rule for the IORs of ash and char lead to appropriate approximations of the radiation behavior of the particle. Furthermore, it is not necessary to model the spatial arrangement of carbon core and ash film for the radiative properties. Modeling a sphere and calculating an effective IOR depending on the carbon, ash, and pore volume fraction results in an average deviation of less than 3 % to the exact solution.

1. Introduction

One of the primary greenhouse gases in earth's atmosphere is carbon dioxide, which stems from the combustion of solid fuels. Since the combustion of solid fuels will continue to contribute significantly to the worldwide energy supply, CO_2-neutral conversion methods are needed. Carbon capture and storage technologies [1], replacing coal by biomass, or a combination of these two options are alternatives for reducing CO_2 emissions from solid fuel-fired power plants. However, designing and developing these technologies and ultimately transferring them to industrial-sized power plants require predictive simulations. The simulation of the combustion process needs to consider various physical phenomena, and thus, the simulation's quality depends on the chosen submodels and their coupling.

A crucial phenomenon for the accurate simulation of the combustion process is radiation. Due to the high temperatures in a combustion chamber, radiation is the most dominant heat transfer mechanism [2]. In case of solid fuel combustion, both, gas and particles contribute to the radiation, and interactions of both radiation phenomena have to be accounted for. Typically, their influence on the energy balance is considered by solving the radiative transfer equation (RTE) [3].

One challenging aspect of solving the RTE is the proper consideration of the highly wavelength-dependent properties of gas radiation. Line-by-line (LBL) integration of the spectral lines provides accurate solutions. However, in the case of solid fuel combustion, about 10^6 RTEs need to be solved. As a result, global models were developed. Instead of solving the RTE with a high spectral resolution, global models consider radiative properties averaged over the entire spectrum while attempting to maintain accuracy. Common global models are the weighted-sum-of-gray-gases model (WSGGM) [4–6] and the full-spectrum correlated-k model (FSCKM) [7]. As gas radiation depends mainly on the temperature of the radiating gas and its concentration, many models were first developed for an air atmosphere. The global

* Corresponding author.
E-mail address: koch@wsa.rwth-aachen.de (M. Koch).

https://doi.org/10.1016/j.fuel.2024.130973
Received 13 November 2023; Received in revised form 8 January 2024; Accepted 11 January 2024

models were adjusted for oxy-fuel conditions [8–10] as the interest in carbon capture and storage technologies has risen. Here, oxy-fuel conditions mean the combustion of solid fuels in an atmosphere of oxygen and carbon dioxide.

Commonly, spectral properties of particles are neglected, and Planck-mean values are applied for the absorption and scattering properties of the particles. Johansson et al. [11] highlighted that particle radiation even dominates gas radiation (for oxy-fuel and air atmospheres), which is supported in later published studies by other researchers [12,13]. This statement was relativized in Guo et al. [14] for coal combustion. They stated that particle radiation dominates the heat transfer near the burner, where the overall particle density is high. Furthermore, particle radiation dominates gas radiation in the burnout region due to the high content of ash particles. In order to distinguish between these two particle types and to be able to calculate the radiative properties, the complex index of refraction (IOR) for coal and ash has to be known.

These two IORs are then applied to the Mie theory [15] to calculate the scattering and absorption properties of the corresponding particle in a combustion chamber. As Mie theory only applies to spherical and homogeneous particles, shape and internal composition of ash and coal particles are simplified. In Gronarz et al. [16], it was shown that assuming a spherical shape for these particles is sufficiently accurate. A follow-up study [17] investigated and verified the homogeneous assumption for coal particles prior to pyrolysis.

Nevertheless, the influence of the conversion process on the radiative properties is rarely considered in simulations of combustion chambers. The particles are assumed to either consist entirely of coal or ash. However, these representations of the particle morphology only represent the start and the end point of the conversion process. During the conversion process, first, the volatiles are released during pyrolysis and a porous char particle remains. Then, the carbon material is converted to gaseous products and released from the particle, while the minerals are transformed into ash. Depending on the reaction conditions and the oxygen transport within the particle pores, effects like ash film formation, particle swelling, and particle shrinking occur. Consequently, the char conversion process can be categorized into three reaction regimes: In regime I, the conversion is limited solely by the intrinsic reaction rate of the char conversion reactions. Enough oxygen is available at all positions within the particle, and the reactions evolve uniformly. In regime II, the conversion process is limited by the oxygen diffusion within the particle pores. Thus, the reactivity is higher at the particle surface than at the center. In regime III, the overall conversion process is limited by the oxygen transport through the boundary layer, and the conversion process only takes place at the particle surface.

Gronarz et al. [18] and Guo et al. [19] used simplified approaches to consider the conversion process on the radiative properties. Gronarz et al. modeled the single particle with a carbon core coated with an ash film, applying the IOR of coal for carbon. Depending on the burnout of the particle, they used a power law to describe the diameter of the core and the total particle. This power law has been derived from the char burnout kinetics model by Hurt et al. [20], which predicts a change in the particle size and its composition during char burnout. To calculate the radiative properties, they applied an extension of the Mie theory, where a shell model for the particle is used [21]. However, this approach did not consider the porosity fraction evoked by the release of volatiles during pyrolysis. In Koch et al. [22], porous particles were modeled, and the influence of porosity and the overall shape on the radiative properties were investigated. They highlighted that the shape of particles and the porosity are not negligible, which indicates the importance of pyrolysis effects on the radiative properties of char particles.

Like Gronarz et al., Guo et al. [19] used the same approach to calculate the total particle and the carbon core diameter. Additionally, they considered the porosity, which was calculated by a correlation based on the CBK model. However, unlike Gronarz et al., they did not apply a shell model. They calculated an effective index of refraction depending on the burnout and, thus, assumed a homogeneous distribution of carbon, ash, and pores during the burnout of the particle.

In contrast to Gronarz et al. and Guo et al., the present study aims to model the particle's composition in dependence on burnout as realistically as possible. For this, the char conversion kinetics (CCK) model [23] calculates the core and particle diameter as well as the ash and pore content. Compared to the CBK model, the CCK model incorporates both gasification and surface oxidation reactions. The output data of the CCK model represent the input to calculate the radiative properties of a single particle — absorption efficiency, scattering efficiency, and scattering phase function. This one-way coupling process is presented in the current study. Furthermore, simplified approaches are compared to this coupling approach. It will be investigated whether it makes a difference in calculating the radiative properties of how the particles react and are structured or whether an effective IOR is sufficiently accurate.

2. Modeling methods

Coupling radiative properties with detailed char conversion kinetics requires modeling different phenomena. The char conversion kinetics (CCK) model calculates the conversion process. While the CCK model is briefly explained, its coupling to the radiation calculations is described in more detail. As the coupling process is implemented via the radiative properties of particles, the calculation of the single radiative particle properties is described, first in general and then for burnout-dependent particles.

2.1. Char conversion kinetics model

The char conversion models incorporate a variety of intricate submodels to capture the essential transport and chemical effects during char conversion. The CCK model [23] combines the 5-step gasification reactions (CBK/G) (with CO_2, H_2O, and H_2) with the 3-step char oxidation reactions (with O_2).

- $2\,C + O_2 \longrightarrow C(O)_\alpha\, CO$
- $C + O_2 + C(O)_\alpha \longrightarrow C(O)_\alpha a + CO_2$
- $C(O)_\alpha \longrightarrow C(O)$
- $CO_2 + C \longleftrightarrow C(O)_\beta + CO$
- $C(O)_\beta \longrightarrow CO$
- $C + H_2O \longleftrightarrow C(O)_\gamma + H_2$
- $C(O)_\gamma \longrightarrow CO$
- $C + 2\,H_2 \longrightarrow CH_4$

Additionally, the CCK model accounts for phenomena including boundary layer diffusion, pore diffusion, ash encapsulation, and thermal annealing. Essential differences between the CCK model and the former CBK model [20] are the updated multiple submodels, which represent more realistic physics and better reproduce the combustion of particles in an oxy-fuel atmosphere. The extended submodels include the swelling model, the annealing model, the mode of combustion parameter, and the kinetic model, complemented by the integration of the chemical percolation devolatilization (CPD) model, which controls the pyrolysis [23].

In this study, the CCK model is used to simulate the burning of a single coal particle in a laminar burner in an oxy-fuel atmosphere. An atmosphere with 20 % O_2, 10 % H_2O, and 70 % CO_2 has been used as boundary conditions [24–26]. The proximate and ultimate analysis of the simulated high volatile bituminous columbian coal is shown in Table 1. The gas temperatures, the wall temperatures as well as other boundary conditions were taken from the experimental results [24–26] and were used in the CCK model.

For the char conversion simulation, the particle is assumed to be spherical with a starting diameter of $D_{P,0} = 100\,\mu m$. Here, the particle

Table 1
Ultimate and proximate analysis of the Colombian coal (hvb coal) investigated: 1 = dry; 2 = daf (dry ash free)

Coal	Volatil. [%m][a]	Ash [%m][1]	C [%m][b]	H [%m][2]	N [%m][2]	O [%m][2]
hvb	36.6	7.7	72.8	5.0	1.9	18.7

[a] Dry.
[b] Dry ash free.

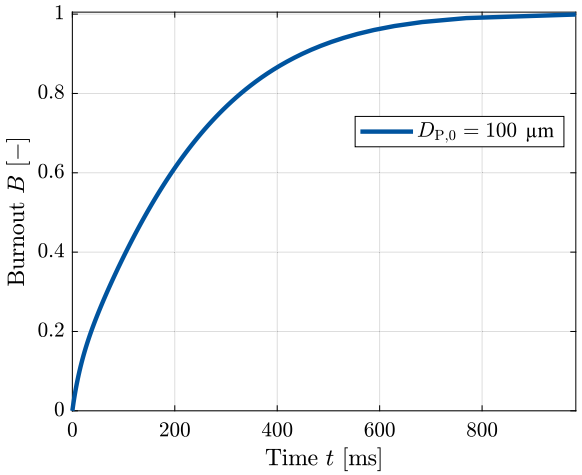

Fig. 1. Burnout depending on the time for $D_{P,0} = 100\,\mu m$.

morphology, material composition, and particle size change within the conversion process. The burnout B is used as a measure for reaction progress and with carbon mass fraction w_c, it is defined as $B = 1 - w_c$. I.e., $B = 0$ indicates the state of the particle after pyrolysis. For $B = 1$, no carbon is left within the particle, and the conversion process is finished. The remaining particle consists of ash with an internal porous structure. Fig. 1 illustrates the burnout B depending on the time t.

The internal structure for $0 < B < 1$ depends on the oxygen transport into the boundary layer and the pores of the particle. Three different conversion regimes arise. These three regimes are illustrated exemplarily in Fig. 2 for $B = 0.1$, $B = 0.5$, and $B = 0.9$.

The particle diameter D_P describes the overall size of the particle. In regime I, the particle size is constant during the conversion process. The conversion proceeds uniformly in the particle, where the carbon content decreases, and the pores increase. The conversion is solely limited by the intrinsic reaction rate (kinetically-limited regime). In regimes II and III, an ash layer with thickness δ_{af} and a core, with diameter D_{core} describe the particle. Furthermore, the particle and core diameter decreases over time. In regime II, the conversion is limited by the oxygen diffusion within the particle pores (pore-diffusion-limited regime). Thus, the reactivity is higher at the particle surface than at the particle core. In contrast to regime II, in regime III, the conversion proceeds only at the surface (film-diffusion-limited regime). Therefore, the volumetric composition of ash, carbon, and pores in the char core is constant in regime III.

Additionally to the internal structure illustrated in Figs. 2, 3 depicts the particle diameter and core diameter in the three regimes as a function of B. In regime II the total particle size shrinks to less than half of its original size, meaning a reduction of the volume by more than 87.5 %, while the core shrinks to approximately a third of the original particle size. However, for $0 < B < 0.4$, the core diameter almost matches the total particle diameter, indicating a small volume fraction of the ash film. In regime III, the overall particle diameter is almost equivalent to the particle diameter in regime II. However, the core is smaller than the particle core in regime II. Therefore, regime III has a more significant ash film than regime II. This behavior is justified by the

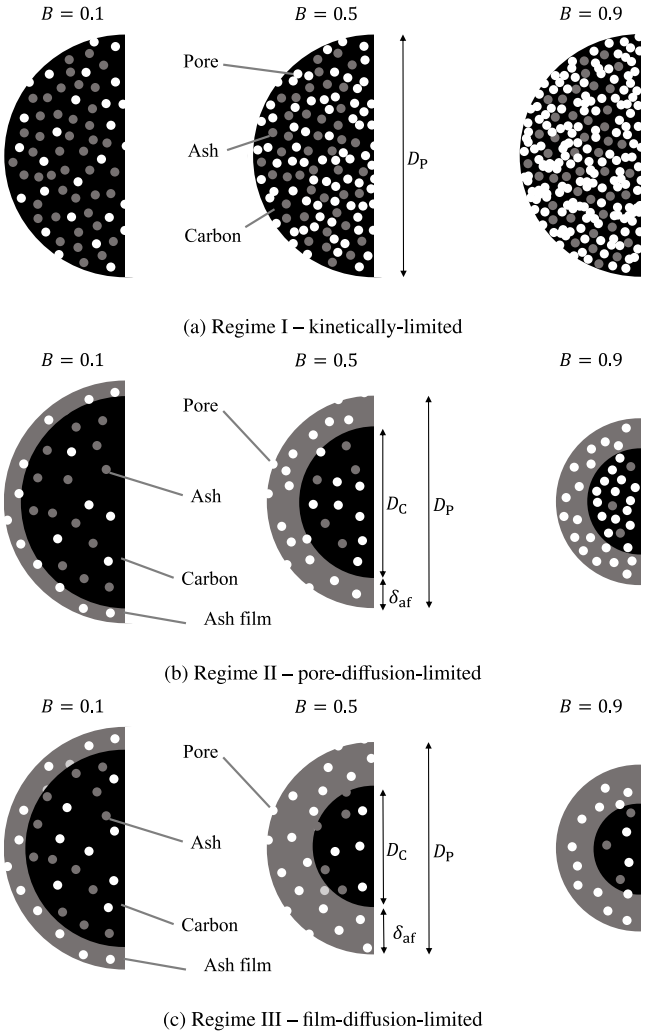

Fig. 2. Illustration of the three regimes for a given burnout. In regime I the particle size is constant and no ash film exists. Difference between regime II and III is a bigger ash film in regime III and a higher porosity in the core for regime II — black illustrates carbon, gray ash, and white pores.

reaction taking only place on the particle surface. Nevertheless, similar to regime II, for $0 < B < 0.4$, the core diameter still almost matches the overall particle diameter. The resulting diameters of regime II are calculated by the CCK-model and the diameters of regime I and III are calculated utilizing the equations in the following subsections using theoretical assumptions.

Coupling process

To calculate the particle-radiation interaction depending on the conversion predicted by the CCK model, the following time-dependent parameters are extracted from the CCK model:

- Ash mass fraction w_a inside the particle
- Total carbon mass fraction w_c of the particle
- Total particle diameter D_P and core diameter D_{core}
- Particle temperature T_P
- Particle porosity Θ_P
- True ash density $\rho_{a,true} = 2650\,kg\,m^{-3}$
- True carbon density $\rho_{c,true} = 2000\,kg\,m^{-3}$

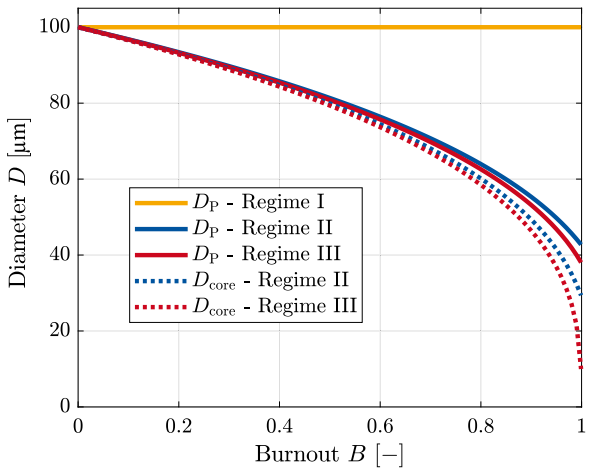

Fig. 3. Diameter depending on the burnout for $D_{P,0}$ 100 µm reacting in the three regimes.

- Particle density at $t = 0\,\mathrm{s}$, $\rho_{P,0} = 1300\,\mathrm{kg\,m^{-3}}$

These parameters are employed to compute the volume fractions of the particle?s porosity, ash, and carbon. These volume fractions are subsequently utilized to determine the radiative properties. As the simulated particle reacted in regime II, the volume fractions are first calculated for regime II. Then, the calculated masses and volumes are used to recreate the particle structure for regimes I and III. The corresponding parameters are indexed with R.I, R.II or R.III to show their relation to regime I–III.

Regime II — pore-diffusion-limited

First, the density of the ash film ρ_{af} is calculated from purely geometric considerations, based on the assumption that there is no loss of ash mass during combustion [27],

$$\rho_{af} = w_{a,0} \cdot \rho_{P,0} \cdot \frac{D_{P,0}^3 - D_{core}^3}{D_P^3 - D_{core}^3} \tag{1}$$

with the total diameter $D_{P,0}$ and ash mass fraction $w_{a,0}$ at burnout state $B = 0$. The ash film density leads then to the ash film porosity:

$$\Theta_{film} = 1 - \frac{\rho_{af}}{\rho_{a,true}} \tag{2}$$

Together with the known particle porosity Θ_P and the ash film porosity Θ_{film}, the pore volume of core and ash film are calculated:

$$V_{film,pore,R.II} = \Theta_{film} \cdot \frac{\pi}{6} \cdot (D_P^3 - D_{core}^3) \tag{3}$$

$$V_{core,pore,R.II} = \Theta_P \cdot \frac{\pi}{6} \cdot D_P^3 - V_{film,pore,R.II} \tag{4}$$

These equations also lead to the ash volume of the film:

$$V_{film,ash,R.II} = \frac{\pi}{6} \cdot (D_P^3 - D_{core}^3) \cdot (1 - \Theta_{film}) \tag{5}$$

As the true ash density is known, the ash volume of the core is calculated utilizing:

$$V_{core,ash,R.II} = w_{a,0} \cdot \frac{\rho_{P,0}}{\rho_{ash,true}} \cdot \frac{\pi}{6} \cdot D_{core}^3 \tag{6}$$

Finally, the necessary volume fractions of regime II are calculated:

$$f_{core,ash,R.II} = \frac{6 \cdot V_{core,ash,R.II}}{\pi \cdot D_{core}^3} \tag{7}$$

$$f_{core,carbon,R.II} = 1 - 6 \cdot \frac{V_{core,ash,R.II} + V_{core,pore,R.II}}{\pi \cdot D_{core}^3} \tag{8}$$

$$f_{core,pore,R.II} = \frac{6 \cdot V_{core,pore,R.II}}{\pi \cdot D_{core}^3} \tag{9}$$

$$f_{film,ash,R.II} = \frac{6 \cdot V_{film,ash,R.II}}{\pi \cdot (D_P^3 - D_{core}^3)} \tag{10}$$

$$f_{film,carbon,R.II} = 0 \tag{11}$$

$$f_{film,pore,R.II} = \frac{6 \cdot V_{film,pore,R.II}}{\pi \cdot (D_P^3 - D_{core}^3)} \tag{12}$$

Regime I — kinetically-limited

For regime I, the burnout-dependent carbon and ash volume of the entire particle is calculated,

$$V_{P,ash,R.I} = V_{core,ash,R.II} + V_{film,ash,R.II} \tag{13}$$

$$V_{P,carbon,R.I} = V_{core,R.II} - V_{core,ash,R.II} - V_{core,pore,R.II} \tag{14}$$

The pore volume $V_{P,pore,R.I}$ results from the pore volume at $t = 0\,\mathrm{s}$ plus the carbon volume that is converted by the reaction. As illustrated in Fig. 3, the overall particle diameter is constant. With these relations, the following volume fractions result:

$$f_{ash,R.I} = \frac{V_{P,ash,R.I}}{\frac{\pi}{6} \cdot D_{P,0}^3} \tag{15}$$

$$f_{carbon,R.I} = \frac{V_{P,carbon,R.I}}{\frac{\pi}{6} \cdot D_{P,0}^3} \tag{16}$$

$$f_{pore,R.I} = \frac{V_{P,pore,R.I}}{\frac{\pi}{6} \cdot D_{P,0}^3} \tag{17}$$

Since, no distinction is made between core and film, only volume fractions for the entire particle are necessary.

Regime III — film-diffusion-limited

As it assumed that there are no reactions taking place within the core, the volume fractions are always constant in the core:

$$f_{core,ash,R.III} = f_{core,ash,R.II}(B = 0) \tag{18}$$

$$f_{core,carbon,R.III} = f_{core,carbon,R.II}(B = 0) \tag{19}$$

$$f_{core,pore,R.III} = f_{core,pore,R.II}(B = 0) \tag{20}$$

Furthermore, it is assumed, that the core volume depends on the burnout and the starting volume as

$$V_{core,R.III} = \frac{\pi}{6} \cdot D_{P,0}^3 \cdot (1 - B) \tag{21}$$

and that the ash film density is the same as in regime II. Thus, utilizing Eq. (1), the particle diameter $D_{P,R.III}$ and the particle volume $V_{P,R.III}$ are calculated. As $\rho_{af,R.III} = \rho_{af,R.II}$, the volume fraction of the ash film also equals the volume fractions of regime II,

$$f_{film,ash,R.III} = f_{film,ash,R.II} \tag{22}$$

$$f_{film,carbon,R.III} = 0 \tag{23}$$

$$f_{film,pore,R.III} = f_{film,pore,R.II} \tag{24}$$

2.2. Radiation interaction with a single particle

If radiation strikes a particle, the radiation is partially absorbed, reflected, refracted, and diffracted. While the absorbed radiation is converted into thermal energy and increases the particle temperature, the remaining effects change the direction of propagation of the interacting radiation. These effects are summed up as effective scattering. In order to quantify the scattered and absorbed radiation by a single particle and consider its size, the radiation areas are introduced. They describe the area on which the radiation is affected due to scattering A_{Sca} or due to absorption A_{Abs}. Typically, these areas are equal to the particle projection area for particles much larger than the wavelength λ of the interacting radiation. However, effects like diffraction have a distinct influence on the overall scattering behavior of the particle for a particle size equal or smaller than the wavelength. Thus, the scattering area A_{Sca} may reach a value larger than the particle projection area

A_P. The radiation efficiencies Q_i (with i = Sca for scattering and i = Abs for absorption) represent the ratio of the virtual interaction area to the projection area and are used to quantify these influences. Similar to the scattering efficiency, the absorption efficiency may also be larger than one [28]. However, the scattering area only indicates the total amount of scattered radiation. To describe the redistribution of scattered radiation into all spatial directions, the scattering phase function Φ is established.

To calculate the radiative properties of a single particle – scattering area, absorption area, and scattering phase function – Maxwell's equations have to be solved for a single, irradiated particle. Usually, numerical methods like the discrete dipole approximation [29] have to be applied, and only in special cases semi-analytical methods like the T-matrix method [30] or analytical solutions exist. For spherical and homogeneous particles, Mie theory [15] yields an analytical solution. For coal or ash particles, it is often used as a benchmark solution to develop more efficient models, and it is also used in this study. For its application, the diameter of the sphere, the complex refractive index of the material (IOR) and the wavelength of the radiation must be known. Since the topic of this study is the radiation interaction with coal and ash particles, the corresponding IOR of these materials is plotted in Fig. 4. The real part n describes the ratio of the speed of light in vacuum to the speed of light in the medium, and the imaginary part k takes into account the absorption strength of the medium.

Typically, data measured by Manickavasagam et al. [31] are used for the IOR of coal. Here, individual coal particles were irradiated, and the scattering pattern was analyzed to determine the IOR. As in these measurements a raw coal particle prior to pyrolysis has been examined, the porosity is negligible. Therefore, this IOR represents in the later calculation the IOR of carbon. For ash particles, the complex IOR measured by Goodwin and Mitchner [32] is used. In comparison to Manickavasagam et al. [31], no scattering experiment was performed. Ash particles were melted and pressed into a thin homogeneous plate. Then the homogeneous plate was irradiated, and the transmitted and reflected radiation was evaluated to determine the IOR of ash.

Based on Fig. 4, the IOR is wavelength dependent. However, there are no extreme fluctuations compared to the radiative properties of gas. Thus, no line-by-line calculations like for the gas radiative properties are necessary and averaging over the relevant spectrum is sufficient. Due to the temperature distribution within a combustion chamber, the relevant wavelength spectrum ranges from 1–10 µm. Over this wavelength range, a Planck-mean value is calculated by applying the following equation:

$$\overline{Q}_i = \frac{\int_\lambda Q_{\lambda,i} \cdot I_B(T_P)\mathrm{d}\lambda}{\int_\lambda I_B(T_P)\mathrm{d}\lambda} \tag{25}$$

with $I_B(T_P)$ representing the temperature-dependent blackbody intensity of the particle and Q the radiation efficiency.

As stated in Section 2.1, the particle is assumed to be spherical and consists of ash, carbon, and pores during the conversion process. As the internal structure is not homogeneous, an extension of the Mie theory is needed, originally derived for coated particles [21]. This extension can model the radiative properties of spherical particles, consisting of a homogeneous core with homogeneous coating, thus, considering two different IORs. In this study, the coating represents the ash film with IOR_{film}, and the core represents the carbon core with IOR_{core}. To consider the ash content and the pores in the core or film, an effective IOR is calculated, applying the following equations,

$$IOR_{film} = f_{ash} \cdot IOR_{ash} + f_{pore} \tag{26}$$

$$IOR_{core} = f_{ash} \cdot IOR_{ash} + f_{carbon} \cdot IOR_{coal} + f_{pore} \tag{27}$$

In Eq. (27), f_i indicates the volume fraction of ash, the pores or carbon to the total volume, which are calculated according to the equations presented in Section 2.1. Fig. 5 illustrates the core volume fractions and Fig. 6 the film volume fractions. For the core, the ash

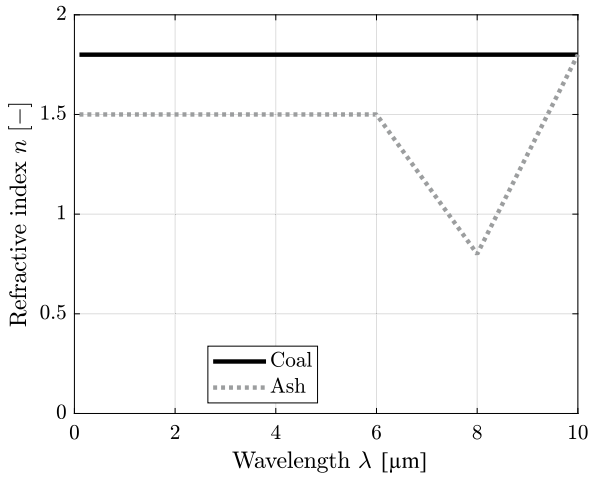

(a) Real part of the complex index of refraction.

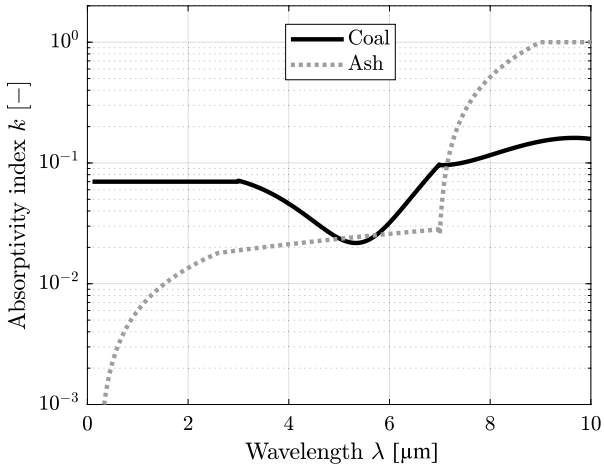

(b) Imaginary part of the complex index of refraction.

Fig. 4. Complex index of refraction of coal and ash. The IOR of coal was measured for individual, cold particles prior to the combustion process [31] and for ash, it was measured from ash particles pressed into a homogeneous, thin plate. [32].

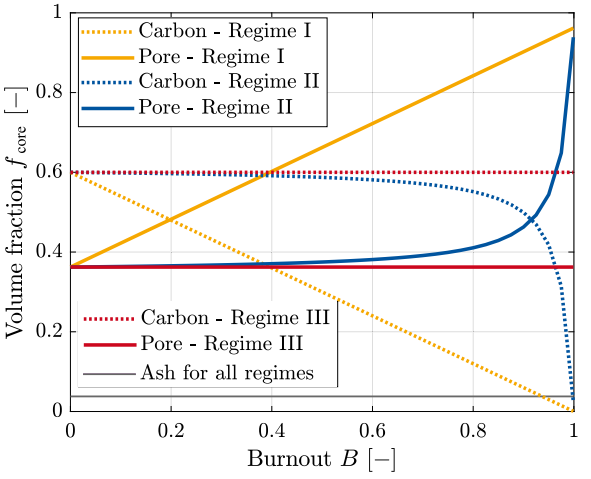

Fig. 5. Volume fractions within the core. The results are calculated for $D_{P,0}$ = 100 µm for regime I–III.

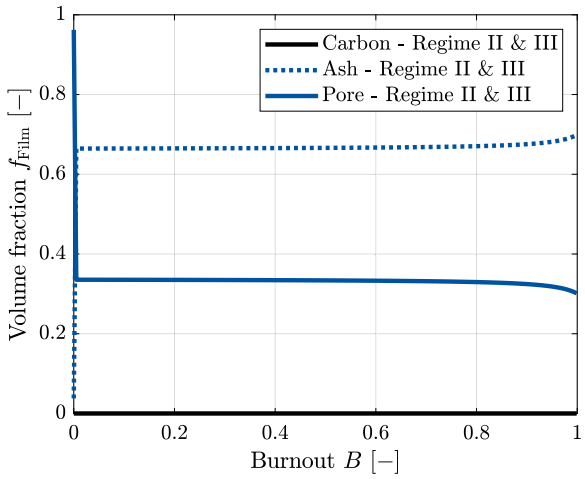

Fig. 6. Volume fractions within the film: Since there is no film in regime I, no volume fractions for regime I are illustrated. The volume fractions of regime III equal the ones of regime II. The results are calculated for $D_{\text{P},0} = 100\,\mu\text{m}$.

volume fraction is constant with $f_{\text{core,ash}} = 0.037$. For regime I, the pore volume fraction increases linearly, and the carbon volume fraction decreases linearly. This relation also means that the IOR of the particle decreases linearly due to Eq. (27). In regime II, the carbon and pore volume fractions are constant for $0 < B < 0.6$ with $f_{\text{core,pore}} \approx 0.35$ and $f_{\text{core,carbon}} \approx 0.6$, respectively. The resulting IOR is also constant since all volume fractions are constant for $0 < B < 0.6$. While the pore volume slowly increases for $0.6 < B < 0.9$ to $f_{\text{core,pore}} \approx 0.5$, the carbon volume fraction reduces to $f_{\text{core,carbon}} \approx 0.45$. Afterward, the pore volume rapidly increases to $f_{\text{core,pore}} \approx 0.97$ for the remaining conversion process, indicating a highly porous core after the conversion process. In regime III, all volume fractions are constant. The decrease in carbon volume causes the overall decrease of the core volume.

The resulting volume fractions of the film are displayed in Fig. 6. Here, only the volume fractions of regime II are displayed, as the regime III volume fractions equal the ones of regime II. The pore volume fraction and the ash volume fraction jump directly to $f_{\text{film,pore}} \approx 0.33$ and $f_{\text{film,ash}} \approx 0.67$. The initial discontinuity is generated by the formation process of the ash film and its implementation in the CCK model. Here, the parameters already integrated in the CCK model play a decisive role. Thus, the ash density, porosity, pore volume from experimental data, and ash particle size were implemented into the CCK model. During almost the entire conversion process, the volume fractions remain constant, and so does the ash film's effective IOR.

3. Results

In this section, the resulting efficiencies, areas and phase functions are compared for the kinetically limited regime (regime I), the pore diffusion limited regime (regime II), and the film diffusion limited regime (regime III). Then the result of simplified approach are compared to these results.

3.1. Radiative properties of particles modeled in regimes I–III

Fig. 7 depicts the resulting absorption efficiency Q_{Abs} and the absorption area A_{Abs} depending on the burnout B. For the regimes II and III, the absorption efficiency shows very similar results. Up to $B = 0.9$, Q_{Abs} remains relatively constant, then decreases rapidly. The rapid change in the value for Q_{Abs} is due to the sudden increase of ash film for $B \geq 0.9$. Additionally, the overall porosity fraction increases for $B \geq 0.9$, which explains the decrease in absorption. In contrast to these results, the results of regime I show a significant deviation due

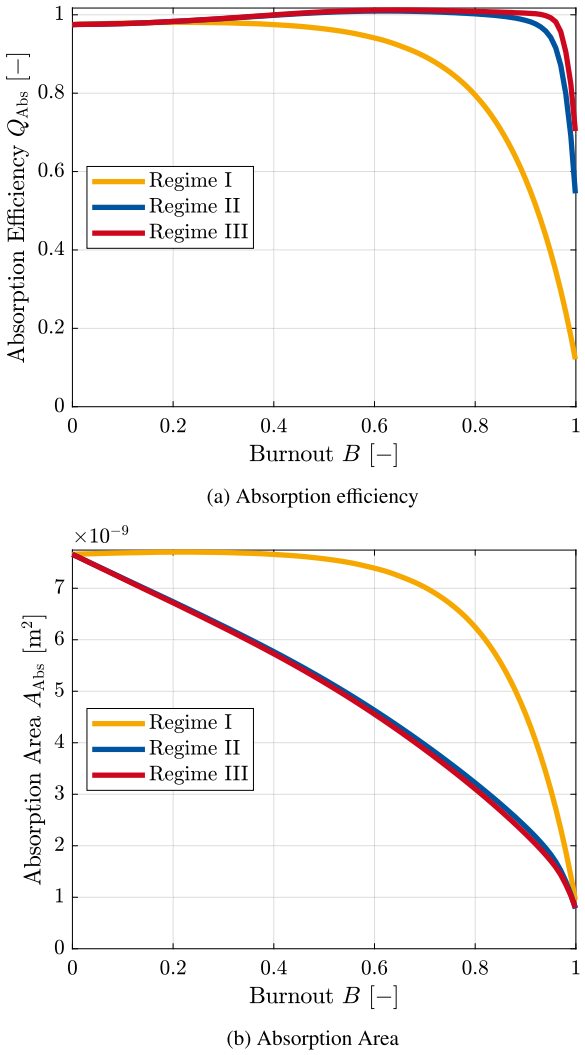

Fig. 7. Absorption efficiency and area as a function of burnout for a starting diameter of $D_{\text{P},0} = 100\,\mu\text{m}$.

to the constant particle size of $D_{\text{P},0} = 100\,\mu\text{m}$. Furthermore, the linear increase in porosity also influences the internal structure and, thus, the absorption efficiency. The absorption efficiency shows a faster decrease for $B > 0.5$, and its final value at $B = 1.0$ is $\approx 10\,\%$ of $Q_{\text{Abs,R.II}}$. Fig. 7(b) displays the Absorption area, which equals the absorption efficiency scaled by the particle area. Here, the absorption area $A_{\text{Abs,R.III}}$ is always larger than the remaining ones. $A_{\text{Abs,R.III}}$ is almost constant for $B < 0.5$, and afterwards, it decreases to the same value as the absorption areas of the other approaches. Particle clouds with the absorption properties of regime III would result in higher radiation absorption and thus in a higher heating rate.

Fig. 8 depicts the results for the scattering efficiency Q_{Sca} and scattering area A_{Sca}. Although, the overall trends of the three regimes are different for Q_{Sca}, similar correlations between regime I, II and III are conducted. Again, regime II and III nearly coincide, and a large difference between regime I to regime II/III is noticed. The only difference is a slightly higher deviation between $A_{\text{Sca,R.II}}$ and $A_{\text{Sca,R.III}}$ for $B > 0.9$. Furthermore, even for $B = 1.0$, $A_{\text{Sca,R.I}}$ does not coincide with the remaining regimes II and III. Particle groups reacting in regime III with higher scattering properties scatter more radiation. This means, that particles at the border of a particle group shield the inner particles better, resulting in less radiation interaction with particles in the middle of particle groups.

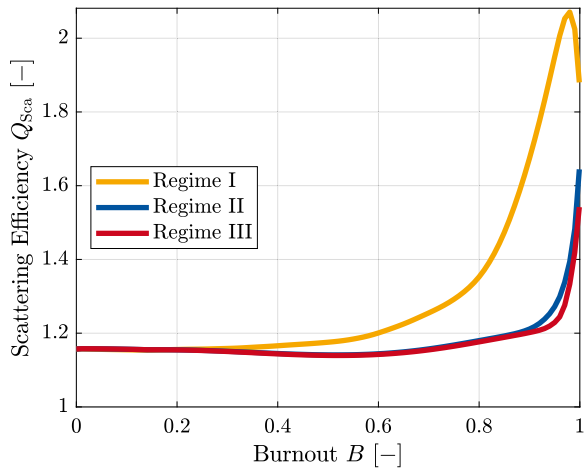

(a) Scattering efficiency

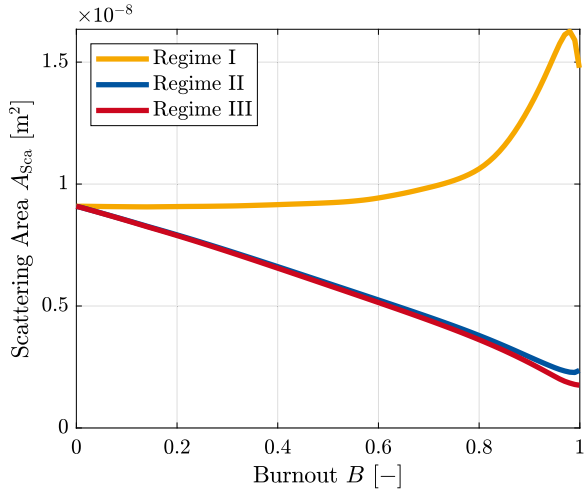

(b) Scattering Area

Fig. 8. Scattering efficiency and area as a function of burnout for a starting diameter of $D_{P,0} = 100\,\mu m$.

The phase functions are illustrated exemplarily for $B \in (0.1, 0.5, 0.9)$ with an initial particle of $D_{P,0} = 100\,\mu m$ in Fig. 9. These plots are evaluated to analyze the effects of burnout and regime dependent modeling on the scattering phase function. The scattering angle θ describes the angle between incident radiation and outscattered radiation. Therefore, $\theta = 0°$ indicates the forward direction, and $\theta = 180°$ indicates the backward direction. For $B = 0.1$, the deviations between the regimes are negligible. The particle size of regimes I, II, and III equals nearly $100\,\mu m$. Thus, even regime I coincides. With increasing burnout, the deviation of regime I increases, due the particle different size and porosity. The phase function indicates pronounced forward scattering and a negligible fraction of backward scattering compared to the other approaches. The results for regimes II and III coincide for all burnouts, similar to the previous results. Only a small deviation in the backscattering is noticed for $B = 0.9$.

All in all, there are no differences between regimes II and III but large deviations between regimes I and II/III. These deviations originate from the size of the particle and its higher porous internal structure. Furthermore, the efficiencies are more sensitive to the changes during the burnout than the phase function since there is almost no difference between the phase functions of regimes II and III. The following section investigates whether it is essential to distinguish between film and core or if a homogeneous distribution of carbon, ash, and pores (like in regime I) is sufficient.

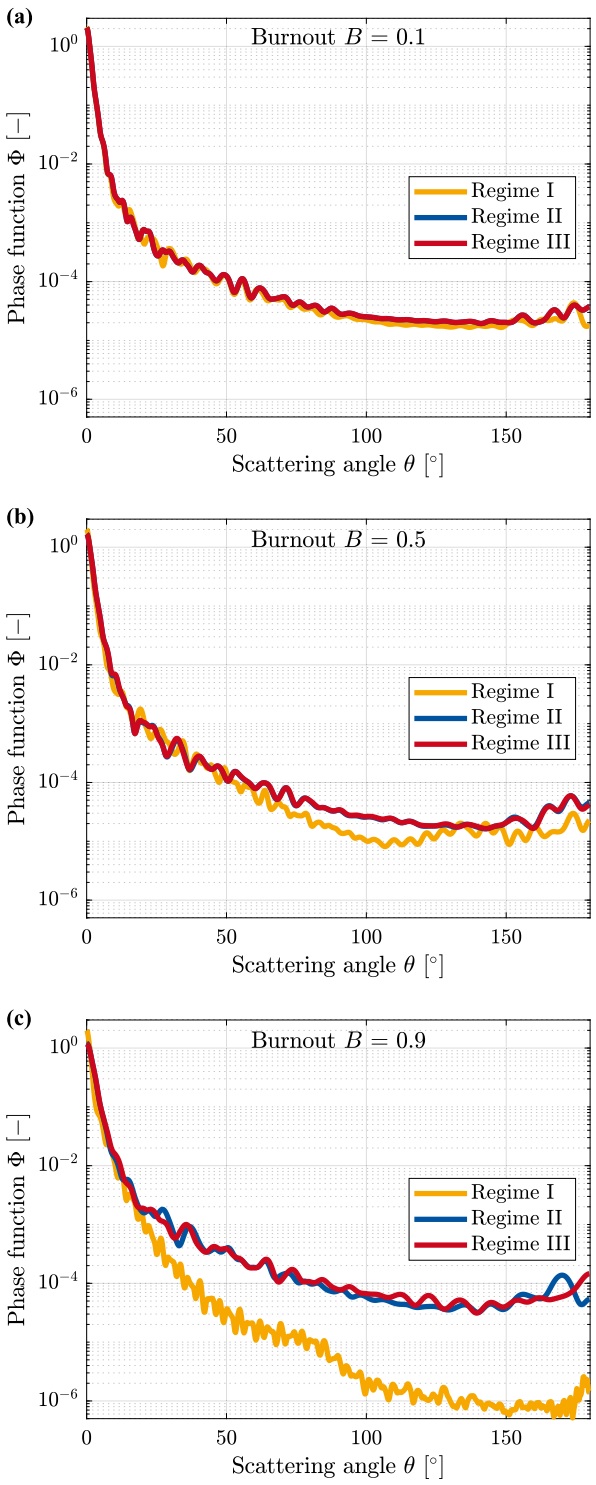

Fig. 9. Scattering phase function for $D_{P,0} = 100\,\mu m$.

3.2. Influence of internal structure on the accuracy

In this section, the radiative properties are additionally calculated for a homogeneous sphere — no film and no core. The particle size and the volume fractions are taken from regime II, and from regime III, respectively. Subsequently, the deviations E between the results of the homogeneous spheres and the coated ones are calculated with Eq. (28), which is exemplarily shown for regime II,

$$E = \frac{Q_{Abs,R.II} - Q_{Abs,R.II,H}}{Q_{Abs,R.II}} \tag{28}$$

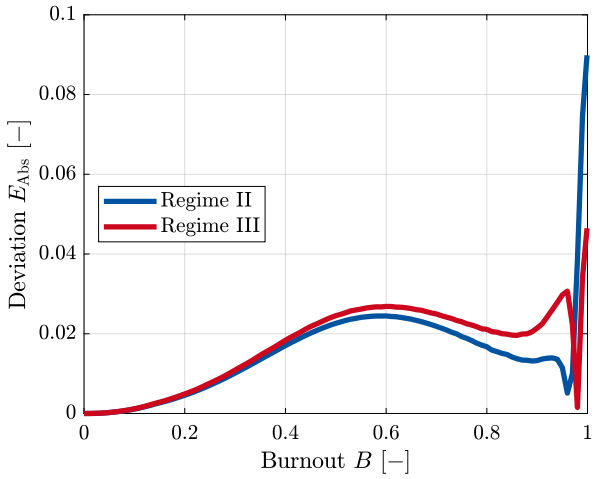

(a) Deviation of the absorption efficiencies

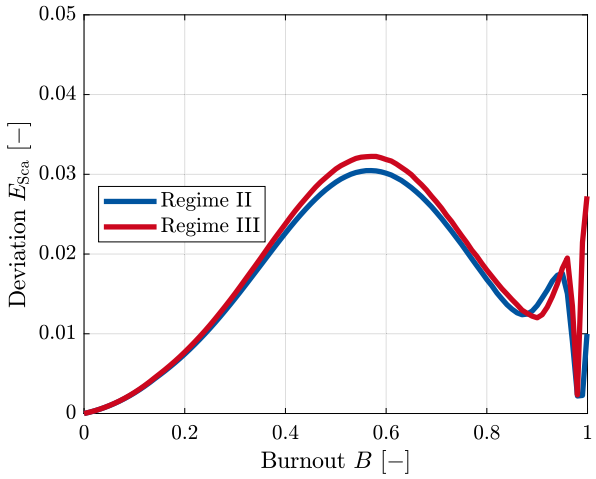

(b) Deviation of the scattering efficiencies

Fig. 10. Deviation of the results approximating the shape and internal structure by a homogeneous sphere or a coated one. Blue indicates the deviation of regime II and red the deviation of regime III. (For interpretation of the references to color in this figure legend, the reader is referred to the web version of this article.)

with $Q_{\mathrm{Abs,R.II,H}}$ representing the efficiency of the homogeneous sphere. The resulting deviations are plotted in Fig. 10(a) and in Fig. 10(b) for the efficiencies. As the ash film size increases with increasing burnout, the deviation also increases. The local maximum deviation is approximately at $B = 0.5$ and decreases afterward. Here, a maximum deviation is reasonable as the ratio between carbon and ash mass is maximal. At $B = 1.0$ the deviation peaks, as the porosity of the core differs from the porosity of the film. However, even for this peak, the deviation is below 10 % and the overall mean deviation is below 10 % (for scattering, absorption, and for regimes II and III). Therefore, it is unnecessary to model the exact internal structure (film & core). Only the particle size and its overall composition are essential. The same findings hold true for the phase function.

3.3. Simplified approaches

In this section, five simplified approaches are suggested for modeling the radiative properties burnout-dependent. A homogeneous sphere is assumed in all approaches, so, there is no distinction between core and ash film; thus, the standard Mie theory is applied. The particle size is taken from regime II, as well as the volume fractions.

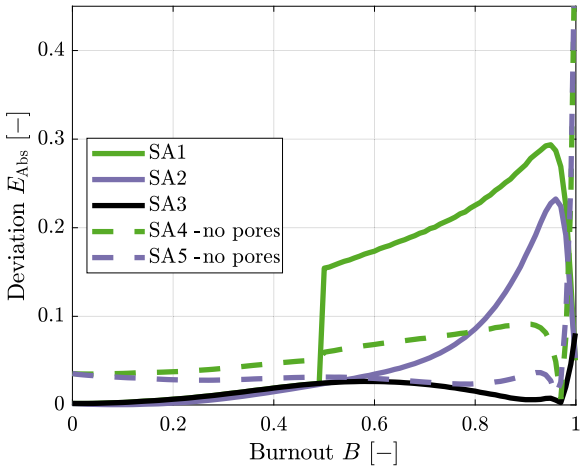

Fig. 11. Deviation of the simplified approaches to the results of regime II calculated by applying $E = \frac{Q_{\mathrm{Abs,R.II}} - Q_{\mathrm{Abs,SA}}}{Q_{\mathrm{Abs,R.II}}}$. (For interpretation of the references to color in this figure legend, the reader is referred to the web version of this article.)

- Simplified approach 1 (SA1)
  $\mathrm{IOR}_{\mathrm{eff}} = \mathrm{IOR}_{\mathrm{coal}} \cdot (1 - f_{\mathrm{pore}}) + f_{\mathrm{pore}}$ for $0 < B < 0.5$
  $\mathrm{IOR}_{\mathrm{eff}} = \mathrm{IOR}_{\mathrm{ash}} \cdot (1 - f_{\mathrm{pore}}) + f_{\mathrm{pore}}$ for $B \geq 0.5$
- Simplified approach 2 (SA2)
  $\mathrm{IOR}_{\mathrm{eff}} = (\mathrm{IOR}_{\mathrm{coal}} \cdot (1 - B) + \mathrm{IOR}_{\mathrm{ash}} \cdot B) \cdot (1 - f_{\mathrm{pore}}) + f_{\mathrm{pore}}$
- Simplified approach 3 (SA3)
  $\mathrm{IOR}_{\mathrm{eff}} = (\mathrm{IOR}_{\mathrm{coal}} \cdot (1 - B^{12.4}) + \mathrm{IOR}_{\mathrm{ash}} \cdot B^{12.4}) \cdot (1 - f_{\mathrm{pore}}) + f_{\mathrm{pore}}$
- Simplified approach 4 (SA4)
  $\mathrm{IOR}_{\mathrm{eff}} = \mathrm{IOR}_{\mathrm{coal}}$ for $0 < B < 0.5$
  $\mathrm{IOR}_{\mathrm{eff}} = \mathrm{IOR}_{\mathrm{ash}}$ for $B \geq 0.5$
- Simplified approach 5 (SA5)
  $\mathrm{IOR}_{\mathrm{eff}} = \mathrm{IOR}_{\mathrm{coal}} \cdot (1 - B) + \mathrm{IOR}_{\mathrm{ash}} \cdot B$

SA4 and SA5 are typically used in CFD simulation. Here, their accuracy is tested. Furthermore, SA1 and SA2 represent SA4 and SA5 considering the pores. SA3 was derived in this study. The exponent 12.4 was derived by minimizing the difference between the results of regime II and SA3 by altering the exponent.

The absorption efficiency deviation is illustrated in Fig. 11. Green indicates SA1, purple SA2, where the dashed line differentiate between the case without pores (SA4 and SA5). Black indicates the results for applying SA3.

SA1, SA2 and SA3 indicate small deviations for $B < 0.5$, while the deviations of SA1 and SA2 increase for $B > 0.5$. The influence of the ash content is overestimated by all three approaches (especially for SA1). Overall, for $B > 0.5$ the mean deviation $\overline{E}_{\mathrm{SA1}}$ is 20.92 %, for $\overline{E}_{\mathrm{SA2}}$ 8.87 % and for $\overline{E}_{\mathrm{SA3}}$ 1.99 %. If the pores are neglected (SA4 and SA5), the overall mean deviation decreases. However, these approaches have a constant set off for the entire conversion process. As the porosity increases for $B > 0.9$ the deviation increases rapidly and reaches deviations larger than 50 %. Only the proposed approach (SA3) indicates for the entire conversion process an adequate approximation of the realistic simulation.

Since SA3 resulted in the slightest deviation from coupling the CCK output with the radiation calculation, Fig. 12 illustrates the deviations of SA3 compared to the deviations of the simplified approaches by Gronarz et al. [18] and Guo et al. [19]. Similar to the approaches neglecting the porosity (cf. Fig. 11), the model by Guo et al. (deviation in red) indicates for $B < 0.5$ a constant offset. This offset results from an underestimation of the particle porosity. With increasing burnout B, the particle porosity predicted by Guo et al. increases, thus decreasing the deviation. However, for $B = 1$, the approach by Guo et al. assumes zero porosity. Therefore, the deviation peaks for $B > 0.9$ to over

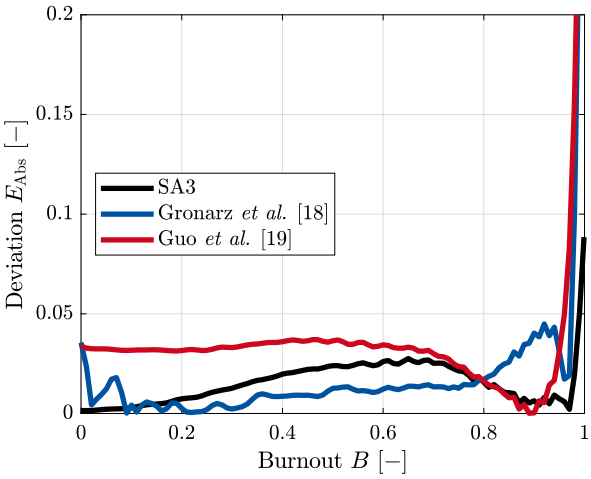

Fig. 12. Deviation of the simplified approach 3 and of the approaches by Gronarz et al. and Guo et al. to the results of regime II calculated by applying $E = \frac{Q_{\mathrm{Abs,R.II}} - Q_{\mathrm{Abs,i}}}{Q_{\mathrm{Abs,R.II}}}$. (For interpretation of the references to color in this figure legend, the reader is referred to the web version of this article.)

$E_{\mathrm{Abs}} = 40\,\%$. Although the model by Gronarz et al. (deviation in blue) neglects the porosity entirely, it indicates slighter deviations than the approach by Guo et al. for $B < 0.8$. The approach by Gronarz et al. approximates the core diameter, the fraction of ash and the carbon diameter more precisely. However, as the porosity fraction is distinctive for an accurate calculation of the radiative properties for $B > 0.9$, the deviation of Gronarz et al. approach peaks also to a value $E_{\mathrm{Abs}} = 40\,\%$.

The scattering phase function was also investigated. However, the deviations of the approaches are negligible, as long as porosity is considered.

3.4. Influence of initial particle diameter $D_{\mathrm{P,0}}$

As explained in Section 2.2, the radiative properties of a single particle depend on its diameter. To evaluate the influence of the initial particle diameter $D_{\mathrm{P,0}}$, the investigations presented in previous Sections 3.1–3.3 are repeated for $D_{\mathrm{P,0}} = 30\,\mu\mathrm{m}$ & $60\,\mu\mathrm{m}$. Similar correlations are conducted, however, the smaller the initial particle diameter, the larger the deviations between the results of the simplified approaches and the results of regime II. The mean deviation for $B > 0.5$ for SA1 is 53.80 %, for SA2 27.11 % and for SA3 0.99 %. Furthermore, the influence of the porosity on the accuracy increases. Here, the overall deviation increases and the peak deviation for $B > 0.9$ increases to $E > 100\,\%$.

4. Conclusion & outlook

In the presented study, the radiative properties of a single particle were calculated considering its conversion process during combustion. For this, the conversion process was calculated by applying the CCK model. Its output was used as input for a modified Mie theory, where a single particle consists of a homogeneous core and a homogeneous coating. The homogeneous core represented the uniform mixing of ash, carbon, and pores, and the homogeneous coating represented the porous ash film. Then, the internal structure of the particle was modeled for three regimes: (1) the conversion evolves uniformly and is solely limited by the intrinsic reaction rate (kinetically limited regime); thus, ash, carbon, and pores are distributed uniformly within the particle — the particle size is constant; (2) the conversion is higher at the particle surface than at the particle center (pore diffusion limited regime) and (3) the conversion only takes place at the particle surface (film diffusion limited regime). For these three regimes, the radiative properties were calculated and compared. Furthermore, five simplified approaches were tested, where two approaches neglected the porosity content.

The following conclusions are drawn:

- With increasing burnout, the absorption efficiency decreases and the scattering efficiency increases. The rapid change for $B > 0.8$ is related to the increase in the highly porous ash film.
- It is not necessary to distinguish between core and film as long as the proper volume fractions are known for the entire particle. Neglecting the porosity yields a constant offset for $B < 0.5$ and the pores influence especially the results for $B > 0.9$. Therefore, all approaches neglecting porosity are not suited for ash particles (or to be precise for $B > 0.9$). This includes the approach by Guo et al., as zero porosity is assumed for the ash particle in their model. All in all, the correct porosity fraction is a mandatory value for modeling radiative properties for $B > 0.9$ and approximating the porosity fraction precisely has to be included even in a simplified approach.
- There are no differences between the results of regimes II and III but large deviations between the results of regimes I and II/III. These deviations originate from the size of the particle and its higher porous internal structure. Therefore, if coupling of the radiative properties to the output of the CCK model is unavailable and a simplified approach is applied, the simplified approach must distinguish between a particle reacting in regime I and regime II/III.
- Simplified approaches to formulate an effective refractive index were tested for regime II. Neither a jump function, where the IOR of coal was used for the entire particle for a burnout $B < 0.5$ and the IOR of ash for $B > 0.5$, nor the linear mixing of the IOR of coal and ash result in an adequate approximation of the efficiencies calculated by the conversion in regime II. Non-linear mixing of the IOR, where the IOR of coal is more dominant during the conversion than the IOR of ash, result in an appropriate approximation. In contrast to the efficiencies, the scattering phase function is less sensitive to errors when modeled by any simplified approach.
- Particles with smaller initial particle diameter $D_{\mathrm{P,0}}$ result in larger deviations of the simplified approaches. Also the influence of porosity fraction on the accuracy is more distinctive.

Although, these results are based on a particle reacting in an oxy-fuel atmosphere, the results and the coupling procedure are transferable to an air atmosphere.

Future work will investigate how the simplified approach affects the full combustion process of an industrial furnace compared to the coupled approach.

CRediT authorship contribution statement

Matthias Koch: Writing – original draft, Visualization, Validation, Software, Methodology, Conceptualization. **Stefan Pielsticker:** Writing – review & editing, Supervision, Investigation. **David Tarlinski:** Writing – review & editing, Writing – original draft. **Viktor Scherer:** Writing – review & editing. **Reinhold Kneer:** Writing – review & editing, Supervision.

Declaration of competing interest

The authors declare that they have no known competing financial interests or personal relationships that could have appeared to influence the work reported in this paper.

Data availability

The datasets presented in this study can be found in: https://doi.org/10.18154/RWTH-2023-09827.

Acknowledgments

This work has been funded by the Deutsche Forschungsgemeinschaft (DFG, German Research Foundation) within the project SFB/TRR 129 Oxyflame (No. 215035359).

References

[1] Chen W-Y, Suzuki T, Lackner M. Handbook of climate change mitigation and adaptation. Cham, Switzerland: Springer International Publishing; 2017.
[2] Bordbar MH, Hyppänen T. Modeling of radiation heat transfer in a boiler furnace. Adv Stud Theor Phys 2007;1(12):571–84.
[3] Chandrasekhar S. Radiative transfer. New York, USA: Dover Publications; 1960.
[4] Denison MK, Webb BW. A spectral line-based weighted-sum-of-gray-gases model for arbitrary RTE solvers. ASME J Heat Mass Transf 1993. http://dx.doi.org/10.1115/1.2911354.
[5] Denison MK, Webb BW. The spectral line-based weighted-sum-of-gray-gases model in nonisothermal nonhomogeneous media. ASME J Heat Mass Transf 1995. http://dx.doi.org/10.1115/1.2822530.
[6] Denison MK, Webb BW. The spectral-line weighted-sum-of-gray-gases model for H_2O/CO_2 mixtures. J Heat Transfer 1995;117(3):788–92. http://dx.doi.org/10.1115/1.2822652.
[7] Modest MF, Zhang H. The full-spectrum correlated-k distribution for thermal radiation from molecular gas-particulate mixtures. J Heat Transfer 2002;124(1):30–8. http://dx.doi.org/10.1115/1.1418697.
[8] Johansson R, Leckner B, Andersson K, Johnsson F. Account for variations in the H_2O to CO_2 molar ratio when modelling gaseous radiative heat transfer with the weighted-sum-of-grey-gases model. Combust Flame 2011;158(5):893–901. http://dx.doi.org/10.1016/j.combustflame.2011.02.001.
[9] Kangwanpongpan T, França FH, da Silva RC, Schneider PS, Krautz HJ. New correlations for the weighted-sum-of-gray-gases model in oxy-fuel conditions based on HITEMP 2010 database. Int J Heat Mass Transfer 2012;55(25–26):7419–33. http://dx.doi.org/10.1016/j.ijheatmasstransfer.2012.07.032.
[10] Bordbar MH, Wkecel G, Hyppänen T. A line by line based weighted sum of gray gases model for inhomogeneous CO_2-H_2O mixture in oxy-fired combustion. Combust Flame 2014;161(9):2435–45. http://dx.doi.org/10.1016/j.combustflame.2014.03.013.
[11] Johansson R, Leckner B, Andersson K, Johnsson F. Influence of particle and gas radiation in oxy-fuel combustion. Int J Heat Mass Transfer 2013;65:143–52. http://dx.doi.org/10.1016/j.ijheatmasstransfer.2013.05.073.
[12] Yin C. Effects of moisture release and radiation properties in pulverized fuel combustion: A CFD modelling study. Fuel 2016;165:252–9. http://dx.doi.org/10.1016/j.fuel.2015.10.057.
[13] Ates C, Selcuk N, Kulah G. Influence of gray particle assumptions on the predictive accuracy of gas property approximations. J Quant Spectrosc Radiat Transfer 2018;220:67–83. http://dx.doi.org/10.1016/j.jqsrt.2018.09.010.
[14] Guo J, Hu F, Jiang X, Li P, Liu Z. Effects of gas and particle radiation on IFRF 2.5 MW swirling flame under oxy-fuel combustion. Fuel 2020;263. http://dx.doi.org/10.1016/j.fuel.2019.116634.
[15] Mie G. Beiträge zur optik trüber medien, speziell kolloidaler metallösungen. Ann Phys 1908;330(3):377–445. http://dx.doi.org/10.1002/andp.19083300302.
[16] Gronarz T, Schnell M, Siewert C, Schneiders L, Schröder W, Kneer R. Comparison of scattering behaviour for spherical and non-spherical particles in pulverized coal combustion. Int J Therm Sci 2017;111:116–28. http://dx.doi.org/10.1016/j.ijthermalsci.2016.08.014.
[17] Gronarz T, Hoeges C, Kez V, Habermehl M, Kneer R. Comparison of scattering behaviour for inhomogeneous particles in pulverized coal combustion. Int J Therm Sci 2019;140:1–7. http://dx.doi.org/10.1016/j.ijthermalsci.2019.02.034.
[18] Gronarz T, Habermehl M, Kneer R. Modeling of particle radiative properties in coal combustion depending on burnout. Heat Mass Transf 2017;53:1225–35.
[19] Guo J, Hu F, Luo W, Li P, Liu Z. A full spectrum k-distribution based non-gray radiative property model for unburnt char. Proc Combust Inst 2019;37:3081–9. http://dx.doi.org/10.1016/j.proci.2018.06.009.
[20] Hurt R, Sun J-K, Lunden M. A kinetic model of carbon burnout in pulverized coal combustion. Combust Flame 1998;113(1–2):181–97. http://dx.doi.org/10.1016/S0010-2180(97)00240-X.
[21] Yang W. Improved recursive algorithm for light scattering by a multilayered sphere. Appl Opt 2003;42(9):1710–20. http://dx.doi.org/10.1364/AO.42.001710.
[22] Koch M, Pielsticker S, Kneer R. Biomass particle radiation interaction and the effect of shape and structure simplifications. In: 12th mediterranean combustion symposium. 2023.
[23] Holland T, Fletcher TH. Comprehensive model of single particle pulverized coal combustion extended to oxy-coal conditions. Energy Fuels 2017;31(3):2722–39. http://dx.doi.org/10.1021/acs.energyfuels.6b03387.
[24] Tarlinski D, Geschwindner C, Li T, Böhm B, Schiemann M. Particle temperature and composition measurements in the ignition phase of single coal particles and particle groups under conventional and oxy-fuel atmospheres. Fuel 2023;332:125894. http://dx.doi.org/10.1016/j.fuel.2022.125894.
[25] Vorobiev N, Valentiner S, Schiemann M, Scherer V. Comprehensive data set of single particle combustion under oxy-fuel conditions, part I: Measurement technique. Combust Sci Technol 2020;1–22. http://dx.doi.org/10.1080/00102202.2020.1743696.
[26] Vorobiev N, Valentiner S, Schiemann M, Scherer V. Comprehensive data set of single particle combustion under oxy-fuel conditions, part II: Data set. Combust Sci Technol 2020;1–16. http://dx.doi.org/10.1080/00102202.2020.1754207.
[27] Gövert B. Char combustion kinetics using a micro fluidized bed reactor (Ph.D. thesis, Dissertation), Rheinisch-Westfälische Technische Hochschule Aachen; 2018.
[28] Bohren CF. How can a particle absorb more than the light incident on it? Amer J Phys 1983;51(4):323–7. http://dx.doi.org/10.1119/1.13262.
[29] Draine BT, Flatau PJ. Discrete-dipole approximation for scattering calculations. JOSA A 1994;11(4):1491–9. http://dx.doi.org/10.1364/JOSAA.11.001491.
[30] Mishchenko MI, Travis LD, Mackowski DW. T-matrix computations of light scattering by nonspherical particles: A review. J Quant Spectrosc Radiat Transfer 1996;55(5):535–75. http://dx.doi.org/10.1016/0022-4073(96)00002-7.
[31] Manickavasagam S, Menguc M. Effective optical properties of pulverized coal particles determined from FT-IR spectrometer experiments. Energy Fuels 1993;7(6):860–9.
[32] Goodwin D, Mitchner M. Flyash radiative properties and effects on radiative heat transfer in coal-fired systems. Int J Heat Mass Transfer 1989;32(4):627–38. http://dx.doi.org/10.1016/0017-9310(89)90211-1.